Third harmonic X-mode absorption in a top-launch configuration on the TCV tokamak

G. Arnoux, S. Alberti, L. Porte, E. Nelson-Melby, J.-P. Hogge and TCV Team

Centre de Recherches en Physique des Plasmas, Asssociation
EURATOM-Confédération Suisse, Ecole Polytechnique Fédérale de Lausanne,
CH-1015 Lausanne, Switzerland

Abstract. In addition to the 2^{nd} harmonic X-mode (X2) electron cyclotron heating (ECH), the TCV ECH system has been completed with three 450 kW gyrotrons operating at the frequency of 118 GHz for 3^{rd} harmonic X-mode (X3) in a top-launch configuration. In the relatively low magnetic field of TCV (1.45 T), the X2 cutoff density is $n_{e,cutoff}^{(X2)} = 4 \cdot 10^{19}$ m^{-3} and X3 extends the accessible plasma density range up to $n_{e,cutoff}^{X3} = 11.5 \cdot 10^{19}$ m^{-3}. The X3 absorption coefficient is lower than that for X2 by a factor $(k_B T_e)/(m_e c^2)$ and a top-launch injection system has been installed to maximize the beam path along the resonance layer, thus maximizing the optical depth. Theoretical considerations based on a 1D slab geometry model show that the X3 absorption depends mainly on the temperature and the density. It is shown, using a simple 2D model, that in the presence of a suprathermal electron population, the resonance layer width is significantly increased owing to the relativistic shift. The specificity of the top-launch configuration implies that the absorption strongly depends on the propagation direction of the beam. Experimental results are compared with calculations using the linear ray-tracing code TORAY-GA. At the maximum available X3 injected power (1350 kW), full single-pass absorption is measured, increasing the global electron energy by a factor 2.5, whereas TORAY-GA predicts only 50% of absorption.

1. Introduction

In the relatively low magnetic field (1.45 T) of the TCV tokamak, the heating and/or current drive capabilities of the 2^{nd} harmonic X-mode (X2) electron cyclotron system operating at 82.7 GHz are limited to plasma densities below the X2 cutoff which is at $n^{X2}_{e,cutoff} = 4.2 \cdot 10^{19}$ m^{-3}. The X2 system is composed of 6 gyrotrons (450 kW each with 2 s pulse length) and the power is injected from the low field side (LFS) with a real time control of the two launcher angles on each launcher [1]. To overcome the X2 density cutoff limitation, the TCV ECH system has been completed with third harmonic X-mode (X3) operating at 118 GHz. The accessible plasma densities are extended up to the X3 cutoff which is $n^{X3}_{e,cutoff} = 11.5 \cdot 10^{19}$ m^{-3}. However, linear theory shows that the X3 wave absorption per unit length is lower than that of X2 by a factor $(k_B T_e)/(m_e c^2)$. Hence, a top-launch injection has been implemented on TCV in order to maximize the optical depth. With this injection scheme, the wave vector $\mathbf{k}$ associated with the X3 wave is such that $\mathbf{k} \cdot \nabla B_\phi \simeq 0$, where B_ϕ is the toroidal magnetic field. In this situation the RF beam trajectory within the vertical resonance layer is maximized, thus maximizing the optical depth.

The X3 top-launch injection scheme was initially proposed by Meyer et al. [2] and TCV is presently the only tokamak that has implemented such a scheme as a main auxiliary electron cyclotron heating system. At low power, the third harmonic absorption properties have been studied by Pachtman at al. in a horizontal LFS injection configuration on the Alcator-C tokamak [3] and by Ségui et al. in a top-launch configuration on Tore Supra [4]. Third harmonic heating ($P_{RF} = 220$ kW) experiments on overdense plasmas in Heliotron DR have been reported by N. Yanagi et al. [5] where it is shown that X3 generates a suprathermal electron population (SEP). The X3 absorption dependence on the density has been investigated by U. Gasparino et al. [6] using a ray-tracing code applied to the LHD geometry. Third harmonic X-mode electron cyclotron emission has been studied by J. N. Talmadge in the Heliotron-E device [7] where the dependence on the temperature is discussed.

This paper is organized as follows. Section 2 discusses the theoretical density and temperature dependence of the X3 absorption coefficient, $\alpha_3^{(X)}$, and the specific features of the top-launch configuration. The absorption in the presence of an SEP represented by a bi-Maxwellian distribution function, calculated by a linear ray-tracing code in the weakly relativistic approximation, is also discussed. The Gaussian beam model used for the linear ray-tracing code TORAY-GA [8, 9, 10] is presented and X3 top-launch absorption in a typical ohmic TCV plasma is shown. Section 3 gives a description of the X3 launcher. Section 4 shows the X3 absorption dependence on the temperature and density as well as its sensitivity to the launcher poloidal angle, where experimental results are compared with TORAY-GA calculations. It is also shown that full single pass absorption can be obtained for X3 wave and that this induces a flattening of the density profile. General conclusions are offered in the last section.

2. Theoretical overview

In this section, the main results of electron cyclotron wave absorption theory are reviewed. The absorption coefficients of X2 and X3 are compared. The impact of the launching geometry on the optical depth hence on the absorption efficiency is discussed. Experimental evidence shows that in the presence of an SEP, X3 absorption is significantly increased. A weakly relativistic absorption calculation including an SEP is performed using a linear ray-tracing code [11] and assuming a bi-Maxwellian electron distribution function. Since most of the experimental results are compared with the linear ray-tracing code TORAY-GA, particular attention is devoted to the modelling of the gaussian beam for the vertical launch.

2.1. Absorption coefficient and 1D slab model

The local absorption properties for a wave propagating perpendicular to the magnetic field, of a given polarization mode (X or O) and a given harmonic n can be described by the absorption coefficient $\alpha_n^{(X,O)}$ [12]. The optical depth τ determines the fraction of absorbed power and is calculated by integrating the absorption coefficient along the beam trajectory in the plasma.

$$\frac{P_{abs}}{P_{inj}} = 1 - \exp\{-\tau\} = 1 - \exp\{\int 2\mathbf{k}'' \cdot \mathbf{ds}\} = 1 - \exp\{\int \alpha ds\} \tag{1}$$

where $\mathbf{k}''$ is the imaginary part of the wave vector and $\mathbf{ds}$ is along the ray path. Assuming a propagation perpendicular to the magnetic field ($\mathbf{k} = \mathbf{k}_\perp$), the absorption coefficient for the third harmonic X-mode in a weakly relativistic model is given by

$$\alpha_3^{(X)} = \left(\frac{3}{2}\right)^4 \left(\frac{\omega_p}{\omega_c}\right)^2 \left(\frac{v_{th}}{c}\right)^2 \left(\frac{\omega_c}{c}\right) \mid 1 + a_3 \mid^2 \cdot N_{\perp,c}^3 \left[- F''_{9/2}(z_3) \right] \tag{2}$$

with

$$a_3 = \frac{\omega_p^2}{3(8\omega_p^2 - \omega_c^2)} \tag{3}$$

where ω_p is the plasma frequency, ω_c is the electron cyclotron frequency, v_{th} is the thermal velocity defined for a Maxwellian distribution function ($v_{th} = \sqrt{(k_B T)/m_e}$), c is the speed of light and

$$N_{\perp,c}^2 = 1 - \left(\frac{\omega_p}{\omega}\right)^2 \frac{\omega^2 - \omega_p^2}{\omega^2(\omega^2 - \omega_c^2 - \omega_p^2)} \tag{4}$$

is the cold refractive index and ω is the angular frequency of the RF wave. F'' is the imaginary part of the Dnestrovskij function [12] which is defined for a given harmonic n such that $F_q(z_n) = F'_q(z_n) + iF''_q(z_n)$ where $q = n + 1/2$ and

$$F_q(z_n) = -i \int_0^\infty \frac{d\tau'}{(1 - i\tau')^q} e^{iz_n\tau'} \tag{5}$$

The argument of the Dnestrovskij function is defined as

$$z_n = \left(\frac{c}{v_{th}}\right)^2 \cdot \frac{\omega - n\omega_c}{\omega} \tag{6}$$

The absorption coefficient for the second harmonic X-mode is given by

$$\alpha_2^{(X)} = \left(\frac{\omega_p}{\omega_c}\right)^2 \left(\frac{\omega_c}{c}\right) \frac{\mid 1 + a_2 \mid^2}{\mid 1 + \frac{1}{2}\left(\frac{\omega_p}{\omega_c}\right)^2 (1 + a_2)^2 F'_{7/2}(z_2) \mid} N'_\perp \left[- F''_{7/2}(z_2) \right] \quad (7)$$

where

$$a_2 = -\frac{1}{2}\left(\frac{\omega_p}{\omega_c}\right)^2 \frac{1 + 3N_\perp^2 F_{7/2}(z_2)}{3 - (\omega_p \omega_c)^2 [1 + \frac{3}{2} N_\perp^2 F_{7/2}(z_2)]}. \quad (8)$$

$N_\perp$ is the real part of the refractive index and is calculated with the hot dielectric tensor. The denominator in Equation (7) comes from the total energy flux (Poynting vector and sloshing flux) and is taken to be 1 for the third harmonic. The expressions for $a_n (n = 2, 3)$ in Equation (7) and Equation (2) are associated with the wave polarization. Since for $n = 3$, $k'' \ll k'$, a_3 can be deduced from the cold dispersion relation whereas for a_2 the hot effects must be taken into account. The finite-Larmor-radius effect appears implicitly in Equation (2) in the term $(v_{th}/c)^2$ and is also contained in the Dnestrovskij function through the argument z_n.

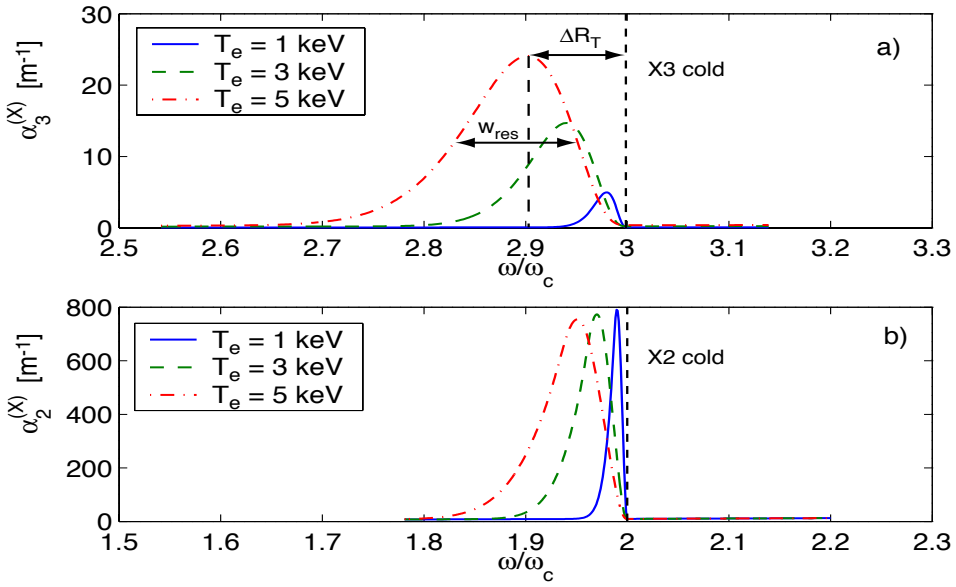

Figure 1. The absorption coefficient is calculated for both X3 (a) and X2 (b) as a function of the normalized cyclotron frequency for three temperatures (1, 3 and 5 keV) and for a density $n_e = 2 \cdot 10^{19}$ m^{-3}. For the third harmonic case, two parameters characterizing the temperature dependence are introduced: the resonance layer width w_{res}, which is taken as the FWHM of α_3, and the shift of the absorption curve ΔR_T, which is taken as the distance between the cold resonance and the maximum of the absorption coefficient $\alpha_{3,max}$.

In order to derive some general results on the absorption properties of the X2 and X3 waves, a simplified 1D slab model is used. Within this model the electron density and temperature are considered spatially homogenous, and the only inhomogeneity is associated with the $1/R$ dependence of the toroidal magnetic field. The effects of the

poloidal field are neglected. Using Equation (7) and Equation (2) in this slab geometry and writing the magnetic field as $B = B_0 R_0/R$ where R is the major radius, R_0 its value at the vessel centre and B_0 the associated magnetic field, Figure 1 shows the absorption coefficient of both third and second harmonics as a function of the magnetic field for typical TCV conditions ($B_0 = 1.45$ T, $R_0 = 0.88$ m, $a = 0.25$ m, $n_{e,0} = 2 \cdot 10^{19}$ m^{-3}) and for three electron temperatures: 1, 3 and 5 keV. As mentioned the ratio between the absorption coefficient of the two harmonics is such that $\frac{\alpha_3^{(X)}}{\alpha_2^{(X)}} \propto \frac{k_b T_e}{m_e c^2}$, that is the $\alpha_3^{(X)}$ curve is proportional to the temperature as can be seen on Figure 1 a). Two other effects associated with the temperature dependence are shown in Figure 1, namely the broadening of the absorption curve $\alpha_{2,3}^{(X)}$ and the shift of the maximum of $\alpha_{2,3}^{(X)}$ towards the high field side (HFS). Due to the relatively weak absorption of the X3 wave, these effects are more significant for the third harmonic and, in order to characterize them, the following parameters are introduced. The broadening effect is characterized by the resonance layer width w_{res} which, as indicated in Figure 1, is defined as the full width at half maximum (FWHM) of the absorption curve. The relativistic shift effect is characterized by the distance ΔR_T between the cold resonance and the maximum of the absorption curve $\alpha_{3,max}$ (see Figure 1). Figure 2 illustrates a third quantity which defines

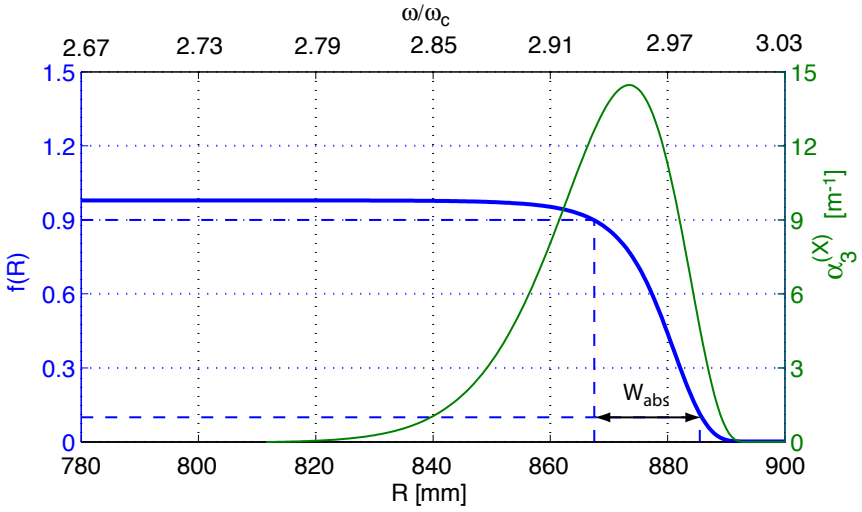

Figure 2. The absorption layer width w_{abs} is defined such that the fraction of the absorbed power $f(R)$ is within 10 % and 90 %. The absorption layer is calculated from the absorption coefficient as a function of R and/or ω/ω_c. In this case, $T_e = 3$ keV and $n_e = 2 \cdot 10^{19}$ m^{-3}, and one find $(\tau_{max,X3}, w_{abs,X3}) = (3.9, 18$ mm) whereas $(\tau_{max,X2}, w_{abs,X2}) = (152, 3.5$ mm).

the characteristic width of the absorption layer w_{abs} for the specific case of horizontal launching from the low field side. This quantity is defined as the horizontal distance between the 10% and 90% values of the normalized absorbed power fraction:

$$f(R) = \frac{1 - \exp[-\tau(R)]}{1 - \exp[\tau_{max}]} \tag{9}$$

where $\tau_{max} = \lim_{R\to\infty} \tau(R)$. For the 2^{nd} harmonic X-mode, $\tau_{max,X2} \gg 1$ whereas for the 3^{rd} harmonic X-mode, $\tau_{max,X3} \simeq 2-3$, for typical TCV parameters. This means that X2 is fully absorbed well before the maximum of α_2 and $w_{abs} \ll w_{res}$ whereas the X3 absorption depends on w_{res} because $w_{res} \simeq w_{abs}$. Figure 3 shows that for typical ohmic TCV plasmas ($T_e = 1$ keV), the X3 absorption fraction P_{abs}/P_{inj} is less than 50% within the density range $3 \cdot 10^{19} \leq n_e \leq 10 \cdot 10^{19}$ m^{-3}. A temperature $T_e = 2.5$ keV must be reached to obtain full single pass absorption in this 1D slab geometry with low field side launching. In order to reach full absorption, the optical depth must be increased by maximizing the beam pass along the resonance. This means that a top-launch configuration is required.

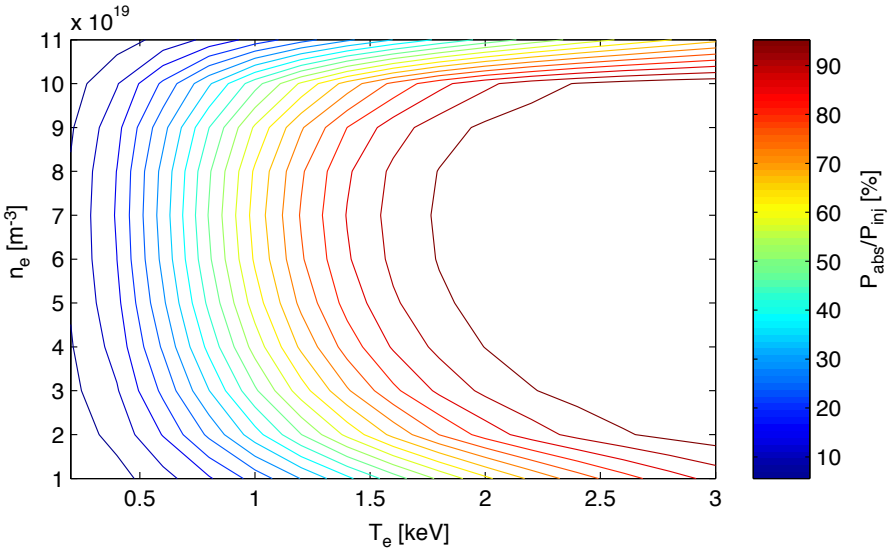

Figure 3. Assuming the 1D slab geometry and using Equation (2), the contour plot of the absorbed power fraction is shown in the density and temperature parameters domain. This shows that X3 wave can be well absorbed ($P_{abs}/P_{inj} \geq 90\%$) within the density range $3 \cdot 10^{19} \leq n_e \leq 10 \cdot 10^{19}$ m^{-3} if the temperature $T_e \geq 2.5$ keV.

Figure 3 shows that X3 absorption also depends on the density. For the X2 and X3 waves, the density dependence of the absorption coefficient is such that

$$\alpha_n^{(X)} \propto g_n(\omega_c, T_e) \cdot h_n(\omega_p, N'_\perp) \tag{10}$$

where $h_3(\omega_p, N'_\perp) = \frac{\omega_p}{\omega_c} \cdot N_\perp^3$ and $h_2 = \frac{\omega_p}{\omega_c} \cdot N'_\perp$ (see Equation (2) and Equation (7)). The cutoff density being defined as $N'_\perp(\omega_{p,cutoff}) = 0$, the absorption coefficient of both harmonics has a maximum between $\omega_p = 0$ and $\omega_p = \omega_{p,cutoff}$. Figure 4 shows this density dependence for both harmonics where, for each harmonic, the function h_n has been normalized to its maximum value. The function $h_2(n_e)$ is maximum when the density is 67 % of $n_{e,cutoff}^{X2} = 4.2 \cdot 10^{19}$ m^{-3} and $h_3(n_e)$ is maximum when the density is 63 % of $n_{e,cutoff}^{X3} = 11.5 \cdot 10^{19}$ m^{-3}. An optimum density range can be arbitrarily defined in the region where $h_3(n_e) \geq 0.6$, which corresponds to $3 \cdot 10^{19} \leq n_e \leq 10 \cdot 10^{19}$ m^{-3}. In this simplified 1D slab model, refraction effects on the ray propagation are not taken

into account. In a 2D system, in particular for the top-launch, such refraction effects can modify the optimum density criteria, especially at high density where refraction is important. These effects will be discussed in section 4.

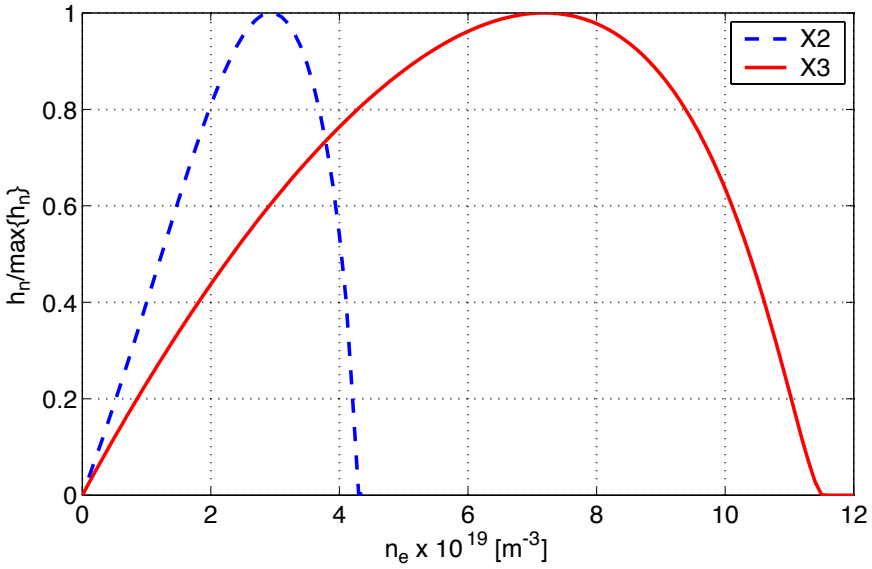

Figure 4. The absorption coefficients of both X2 and X3 depends on the density via the function $h_n(n_e)$ defined in Equation (10). The functions h_2 (blue dashed line) and h_3 (red plain line) are normalized to their maximum value and vanish at the cutoff density: $4.2 \cdot 10^{19}$ m^{-3} and $11.5 \cdot 10^{19}$ m^{-3} respectively.

As shown in Figure 1 and Equation (2), for a fixed density and magnetic field profile, the absorption curve α_3 has a temperature dependence which is parametrized by the quantities ΔR_T and w_{res}. The shift ΔR_T of $\alpha_{3,max}$ toward the HFS and the broadening of w_{res} can be related, in a top-launch configuration, to the launcher poloidal angle θ_l defined in Figure 5 c). Neglecting the refraction effects in the 1D slab model, the broadening of w_{res} translates into a launcher poloidal angle tolerance $\delta\theta_l$ (see Figure 5 a)), while the ΔR_T shift of $\alpha_{3,max}$ must be followed by the launcher via a correction $\Delta\theta_l$ (see Figure 5 b)) with respect to a vertical launch ($\theta_l = 45^o$). Using this simple geometry and taking the distance between the launcher and the plasma center to be $\Delta z = 800$ mm, for typical TCV plasmas, the two angles $\Delta\theta_l(\Delta R_T)$ and $\delta\theta_l(w_{res})$ are small and can be approximated by: $\Delta\theta_l = \frac{1}{2}\frac{\Delta R}{\Delta z}$ and $\delta\theta_l = \frac{1}{4}\frac{w_{res}}{\Delta z}$. The first quantity $\Delta\theta_l$ is a net aiming variation of the launcher angle so as to reach the maximum absorption, whereas the quantity $\delta\theta_l$ defines an aiming accuracy around the optimal angle $\theta_{l,opt} = 45^o + \Delta\theta_l$. The temperature dependence of these two quantities, for the TCV geometry, is such that $\frac{d}{dT_e}(\delta\theta_l) = 0.15$ deg/keV and $\frac{d}{dT_e}(\Delta\theta_l) = 0.25$ deg/keV as shown in Figure 6. The shift dependence implies that $\alpha_{3,max}$ moves such that $\frac{d}{dT_e}(\Delta R_T) = 8$ mm/keV. The launcher tolerance $\delta\theta_l$ will be compared in the following sections with ray-tracing calculations and experimental results. The angular tolerance is directly linked to the resonance layer width and the following subsection discusses the effect of supra-thermal electrons on the absorption of top-launched X3 waves.

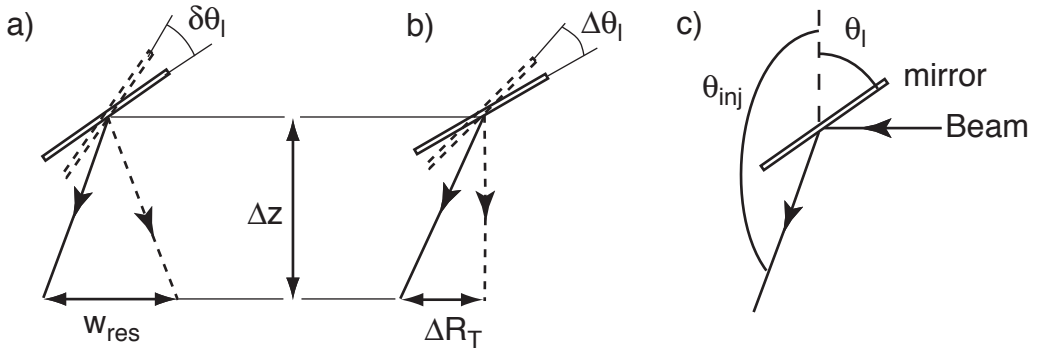

Figure 5. a) The launcher angle tolerance is evaluated using the resonance layer width w_{res} and a typical vertical distance between the launcher and the plasma center Δz, b) The launcher angle correction $\Delta\theta_l$, due to the shift ΔR_T, is taken with respect to the vertical launch ($\theta_l = 45^o$) which is assumed to follow the cold resonance. c) The relation between the injection angle θ_{inj} and the launcher angle is such that $\theta_{inj} = 3\pi/2 - 2\theta_l$.

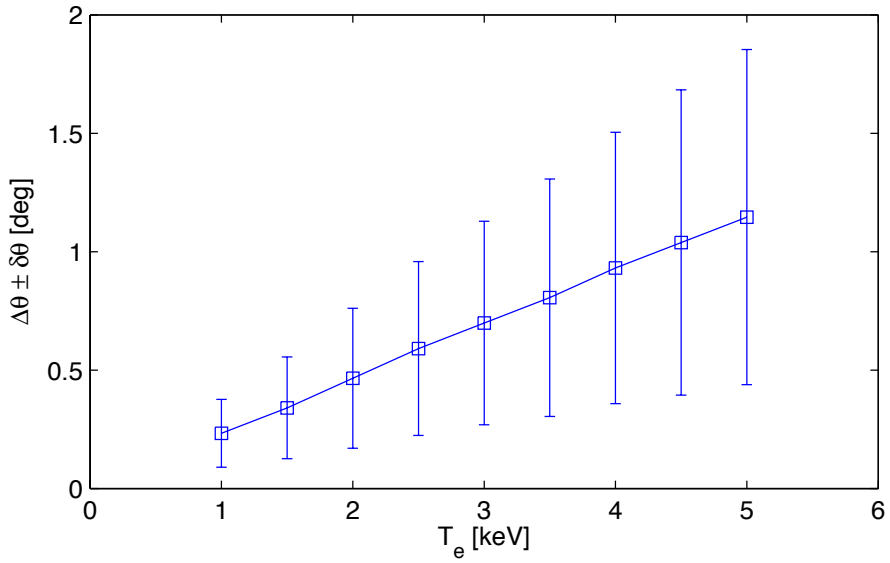

Figure 6. The shift ΔR_T of the maximum absorption coefficient $\alpha^{(X)}_{3,max}$ depends on the temperature and requires a correction $\Delta\theta_l$ of the launcher poloidal angle with respect to the vertical injection. At the same time, the required accuracy on the launcher poloidal angle associated with the temperature increase decreases ($\delta\theta_l$ increases).

2.2. Bi-Maxwellian distribution function

Previous experiments [13] performed on TCV injecting the X3 wave from the LFS in the presence of X2 electron cyclotron current drive (CO-ECCD) preheating have shown that full single pass absorption can be obtained due to a significant fraction of the X3 wave being absorbed by an SEP generated by the X2 wave. Accordingly, in a top-launch

configuration, the absorption properties of the X3 wave can also be significantly modified in the presence of an SEP generated by X2 wave or by the X3 itself. This subsection discusses the properties of the X3 top-launch in a 2D model that incorporates an SEP through the simple approximation of a bi-Maxwellian distribution function: $f(\mathbf{r},\mathbf{v})$ is defined as a linear combination of two Maxwellians such that $f = (1-\eta)f_b + \eta f_s$ [14] where $f_b(\mathbf{r},\mathbf{v})$ represents the bulk, which is characterized by a temperature $T_{e,bulk}(\mathbf{r})$ and a density $n_{e,bulk}(\mathbf{r})$, and $f_s(\mathbf{r},\mathbf{v})$ represents the SEP, which is characterized by a temperature $T_{e,sup}(\mathbf{r})$ and a density $n_{e,sup}(\mathbf{r})$. The distribution functions are normalized such that $\int f_b(\mathbf{r},\mathbf{v})d^3v = \int f_s(\mathbf{r},\mathbf{v})d^3v = 1$ and the suprathermal and bulk densities are related through the expression

$$n_{e,sup} = \frac{\eta}{1-\eta} n_{e,bulk}. \tag{11}$$

The ray-tracing code used in [11], based on a cold plasma model, is used for calculating the absorption along the ray path. Spatial inhomogeneities in the magnetic field as well as in the electron densities and temperatures are taken into account.

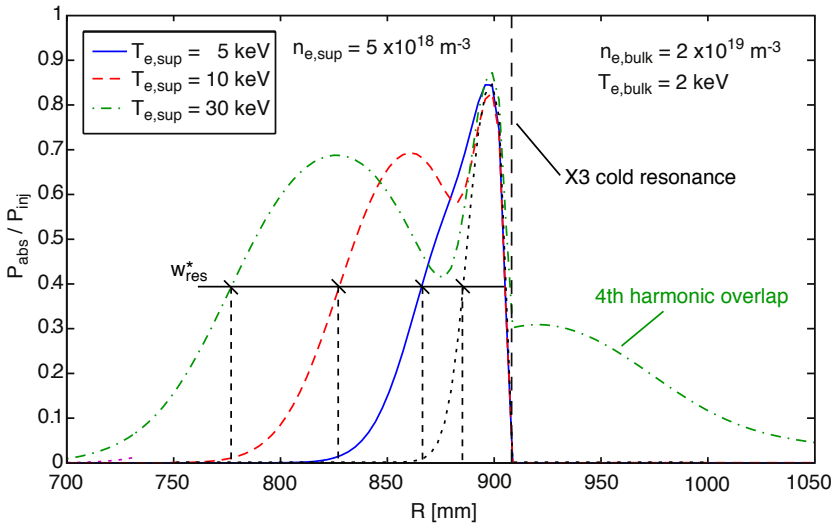

Figure 7. The X3 single-pass absorption P_{abs}/P_{inj} is calculated along a single vertical ray as a function of the launcher radial position R. Each ray starts from the top with injection angle $\theta_{inj} = 180^o$, which corresponds to vertical launch. The distribution function is assumed to be bi-Maxwellian with a central bulk temperature $T_{e,bulk} = 2$ keV, a central bulk density $n_{e,bulk} = 2 \cdot 10^{19}$ m^{-3} and a suprathermal density $n_{e,sup} = 5 \cdot 10^{18}$ m^{-3}. The suprathermal temperature $T_{e,sup}$ is varied from 0 to 30 keV.

Assuming the bi-Maxwellian distribution function described above, calculations of X3 absorption have been performed using a weakly relativistic model. It was shown in [11] that in most cases, there is no synergy between the two components of the bi-Maxwellian distribution function, that is: $\eta_{abs}(f_b + f_s) \simeq \eta_{abs}(f_b) + \eta_{abs}(f_s)$ where η_{abs} is the fraction of absorbed power. Figure 7 shows the single-pass absorption of a single ray (no diffraction effects) as a function of the launcher radial position R. To

model a purely vertical launch, the injection angle θ_{inj} is set to 180^o for each R. In the present case, ray-tracing calculations have shown that the whole ray trajectory can be considered as straight and vertical. The bulk temperature and density profiles are parabolic fits on Thomson scattering measurements on a typical plasma target used in X3 experiments. The plasma is assumed to be circular to simplify the magnetic surfaces, and Shafranov and diamagnetic effects are taken into account. The equilibrium is not representative of TCV plasmas but it gives a good estimation of the effect of the SEP on the X3 absorption. For the suprathermal population, the density profile is taken to

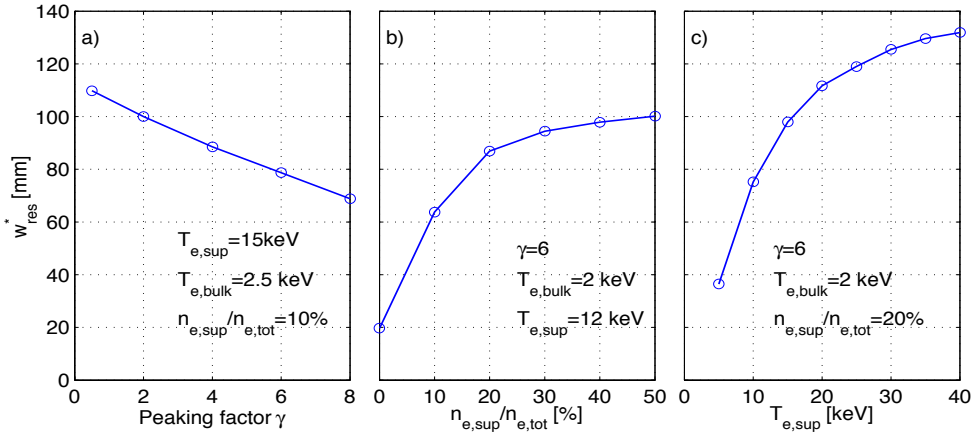

Figure 8. The dependence of the resonance layer width w^*_{res} on (a) γ, the peaking factor of the suprathermal temperature profile, (b) the density ratio $n_{e,sup}/n_{e,tot} = \eta$, (c) the suprathermal temperature $T_{e,sup}$.

be $n_{e,sup}(\rho) = n_{e,sup}(1-\rho^2)^\gamma$ where $\rho = \rho_\psi$ is the normalized flux coordinate, $\gamma = 6$ is the peaking factor (estimated in TCV [14]) and in the case of Figure 7, $n_{e,sup} = 5 \cdot 10^{18}$ m^{-3}. In previous experiments combining X2 ECCD and X3 ECH with X3 launched from the LFS [13], the SEP maximum density and temperature were measured up to $5 \cdot 10^{18}$ m^{-3} ($n_{e,sup}/n_{e,tot} = 20\%$) and 12 keV respectively [14]. Taking into account the spatial distribution of this SEP [14], the ratio between the SEP and bulk electron energy $W_{e,sup}/W_{e,bulk} = 30\%$. The value of $T_{e,sup} = 30$ keV in Figure 7 is only given to illustrate the effect of the harmonic overlap when such a high SEP energy would be genearted. This density, which correspond to 20% of the total density, is not representative of TCV plasmas and has been chosen so high to underline the effect of the SEP and not to make quantitative predictions. The suprathermal temperature is varied from $T_{e,sup} = 0$ to $T_{e,sup} = 30$ keV and the $T_{e,sup}$ profiles are assumed to be flat [14]. The SEP significantly broadens the absorption layer width w^*_{res} defined as the FWHM of the curves shown in Figure 7. Note that if the suprathermal temperature $T_{e,sup} \geq 20$ keV, the 4^{th} harmonic contributes to the resonance layer width broadening on the LFS of the cold resonance. Notice that even for $T_{e,sup} = 0$ (no SEP) $w^*_{res} \neq w_{res}$ (see subsection 2.1) since w^*_{res} includes the $1/R$ dependence of the magnetic field as well as the poloidal field component and also refraction effects on the ray trajectory. The w^*_{res} broadening due

to the SEP depends mainly on three parameters as can be seen in Figure 8. Figure 8 c) shows the w^*_{res} dependence on the suprathermal temperature for the same conditions as in Figure 7 where $n_{e,sup}$ is such that $\eta = 0.2$. The broadening effect is especially strong in the range $5 \leq T_{e,sup} \leq 20$ keV over which the resonance layer width is increased by a factor 3. This is the suprathermal temperature typically estimated in TCV experiments. Thus the SEP can significantly change the X3 top-launch absorption properties in some scenarios. The relative density $\eta = n_{e,sup}/n_{e,tot}$ of suprathermal electrons is important. In Figure 8 b), 10% of suprathermal electrons at a temperature of $T_{e,sup} = 12$ keV can broaden the resonance layer width by a factor 3. Compared with the X3 beam waist in TCV ($w_0 = 23$ mm) 5% of suprathermal electrons give a resonance layer of the same size as the beam. This must be taken into account in the study of the angular tolerance $\delta\theta_l$ on the launcher poloidal angle. Figure 8 a) shows that the $n_{e,sup}$ profile peaking factor does not affect significantly the broadening effect in comparison to the two others parameters. For X3 experiments presented in section 4, it is necessary to keep in mind that the suprathermal electrons can hardly modify absorption properties in the HFS region of the cold resonance because this affects the interpretation of most of the experimental results.

2.3. Beam modeling for top-launch injection

Neglecting any refraction effects, the RF beam propagation can be described by the lowest order eigenmode of a free-space propagating EM wave that has a gaussian transverse profile of the electric field. For this mode, the beam power density is also gaussian and is characterized by its minimum waist w_0 defined by

$$P(r) = P_0 \exp\left\{-\frac{r^2}{w_0^2}\right\} \tag{12}$$

where r is the transverse coordinate perpendicular to the wave vector $\mathbf{k}$.

For LFS injection in ECH, the wave vector $\mathbf{k}$ being nearly $\perp$ to the vertical resonance, the absorption properties can be considered independent of w_0. On the contrary, for the top launch where $\mathbf{k} \parallel \nabla B$, i.e. $\mathbf{k} \parallel$ to the resonance layer, the absorption strongly depends on the ratio w_0/w^*_{res}. This dependence requires a proper description of the gaussian beam profile if a ray-tracing model is to be used.

TORAY-GA is a linear ray-tracing code that calculates the single pass absorption along the ray trajectory of a RF wave. In the case of X3 ECH, the ray trajectory is calculated using the cold dispersion relation because the imaginary part of the wave vector $k'' \ll k'$ where k' is the real part of the wave vector. The gaussian beam is modeled by an appropriate distribution of rays each carrying the same power (see Figure 9). Diffraction effects cannot be described by a ray-tracing model and, in order to best approximate the gaussian propagation in the actual geometry in TCV where the variation of the spot size along the beam is weak (the beam is focused on the center of the vessel), the beam is considered as collimated (no divergence due to diffraction), i.e. each ray starts with the same initial angle.

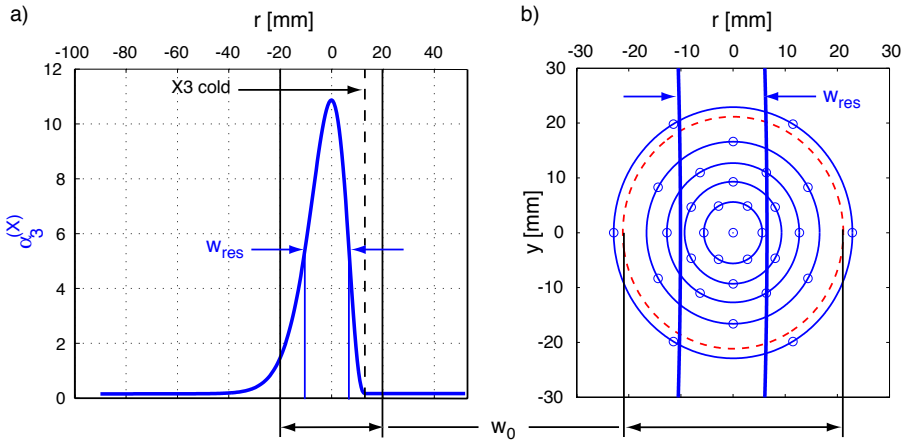

Figure 9. a) w_{res}, determined from $\alpha_3^{(X)}$ calculated for $T_e = 2$ keV and $n_e = 4 \cdot 10^{19}$ m^{-3}, is compared to the X3 beam waist w_0. b) The ray distribution (small open circles) over the beam cross-section, where $N_{rays} = 6$, $N_c = 5$ and $N_{tot} = 31$, used in the gaussian beam model. The beam waist, w_0 (dashed line) is also shown.

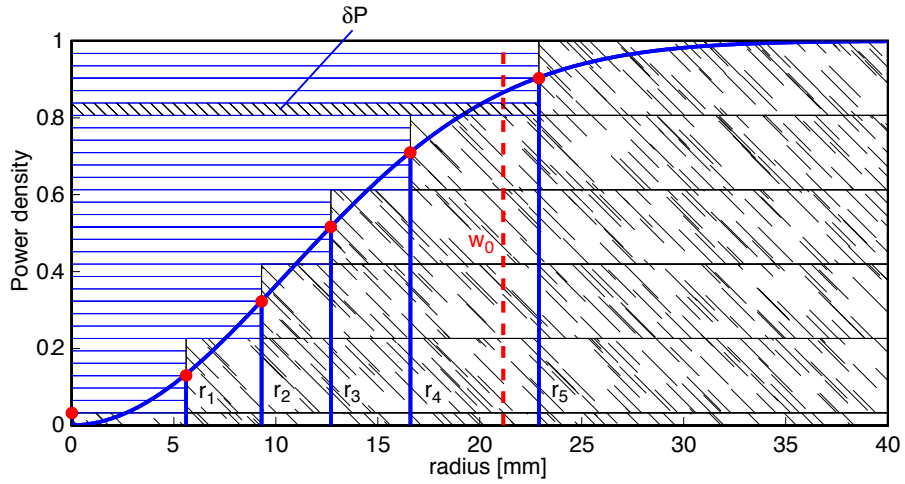

Figure 10. The radial distribution of the rays is such that each ray (here $N_{tot} = 31$) carries an equivalent fraction δp of the total power. The number of rays, for a given radius r_i ($N_{ray} = 6$ in each large shaded rectangle) is chosen and determines the number of circles ($N_c = 5$). To each set of rays (large shaded rectangles) corresponds a radii r_i (full circles) according to the power density (see Equation (13)).

The ray distribution on the beam cross section is generated in two steps: first the radial distribution and second the azimuthal distribution. For a fixed number of rays N_{tot}, the total power is subdivided in N_{tot} equivalent parts so that each ray carries the same power δP (small shaded rectangle in Figure 10). The number of rays $N_{ray}(k)$ carried by each radius is then chosen. Figure 9 shows the corresponding circles and

their radius. According to the power density, the radius r_i is such that

$$\Big[1+\sum_{k=1}^{i}\cdot N_{ray}(k)\Big]\delta P = 2\pi\int_0^{\alpha_i} rP(r)dr \quad where \quad \alpha_i=(r_i+r_{i+1})/2, \quad i=1\ldots N_c (13)$$

This type of radial distribution is used for every TCV launcher. For the top-launch case, since an homogeneity in the azimuthal distribution has to be ensure (it will be described how below), the number of ray per radii r_i has to be kept constant $N_{ray}(k) = Cst \quad \forall k$. This leads to a restriction on the choice of the total number of rays: $N_{tot} = N_{ray} * N_c + 1$. As shown in Figure 9 b), we chose $N_{ray} = 6$ and $N_{tot} = 31$ implying $N_c = 5$ (each circle corresponds to a large shaded rectangles in Figure 10). The rays on each circle are placed at an equivalent distance corresponding with an angle of 60^o and good azimuthal symmetry is obtained when the rays on one circle are rotated by 30^o with respect to the previous one. Figure 9 b) compares the ray distribution with the resonance layer width defined in Figure 9 a) and shows the necessity of having a homogeneous azimuthal distribution since 50% of the rays are outside the resonance layer.

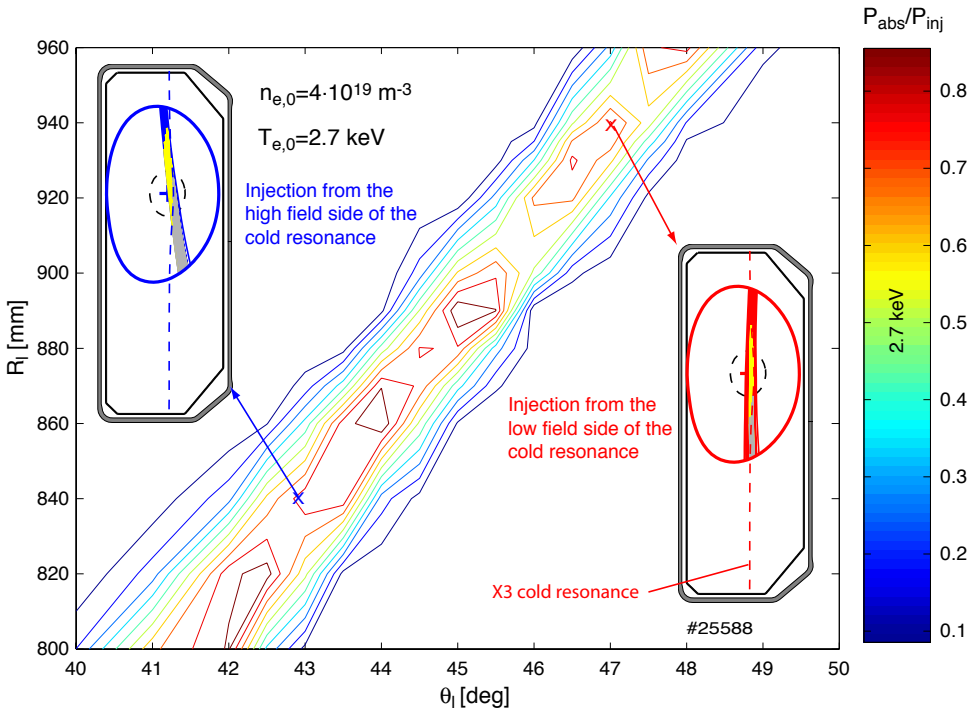

Figure 11. The contour plot of the absorption calculated by TORAY-GA in the X3 launcher parameter space, R (radial position) and θ_l (poloidal angle), shows that an optimal angle $\theta_{l,opt}$ can be found for any R within the accessible range. The poloidal views of TCV in the figure corners show the calculated beam trajectories for two different values of $\theta_{l,opt}$.

An overview of TORAY-GA calculations using a typical X3 plasma target is presented in Figure 11. For the X3 top-launch geometry, the absorbed power fraction P_{abs}/P_{inj} is shown as a function of the launcher parameters (R, θ_l) (see section 3)

where the central temperature and density are $T_{e,0} = 2.7$ keV and $n_{e,0} = 4 \cdot 10^{19}$ m^{-3}, and no SEP is considered. The X3 cold resonance is located at $R_{cold} = 890$ mm and the launcher poloidal angle $\theta_l = 45^o$ corresponds to a vertical launch. For radial positions of the mirror located either in the HFS ($R_l < R_{cold} \Rightarrow \theta_l < 45^o$) or in the LFS ($R_l > R_{cold} \Rightarrow \theta_l > 45^o$), the ray trajectories are shown in the inserts. As expected, for all values of R_l the absorption strongly depends on θ_l and an optimal angle $\theta_{l,opt}$ can be found allowing 80% absorption if $T_{e,0} = 2.7$ keV. Figure 12 shows the P_{abs}/P_{inj} dependence on the temperature and the density. The magnetic equilibrium is the same as in the previous figure and the profiles are the fits to the Thomson scattering measurements in Figure 20. The profiles have been multiplied by an appropriate factor to cover the region $3 \cdot 10^{19} \leq n_{e,0} \leq 8 \cdot 10^{19}$ m^{-3} and $1 \leq T_{e,0} \leq 3$ keV. Note that the density profile is not monotonic, thus the central density is not the maximum density. As

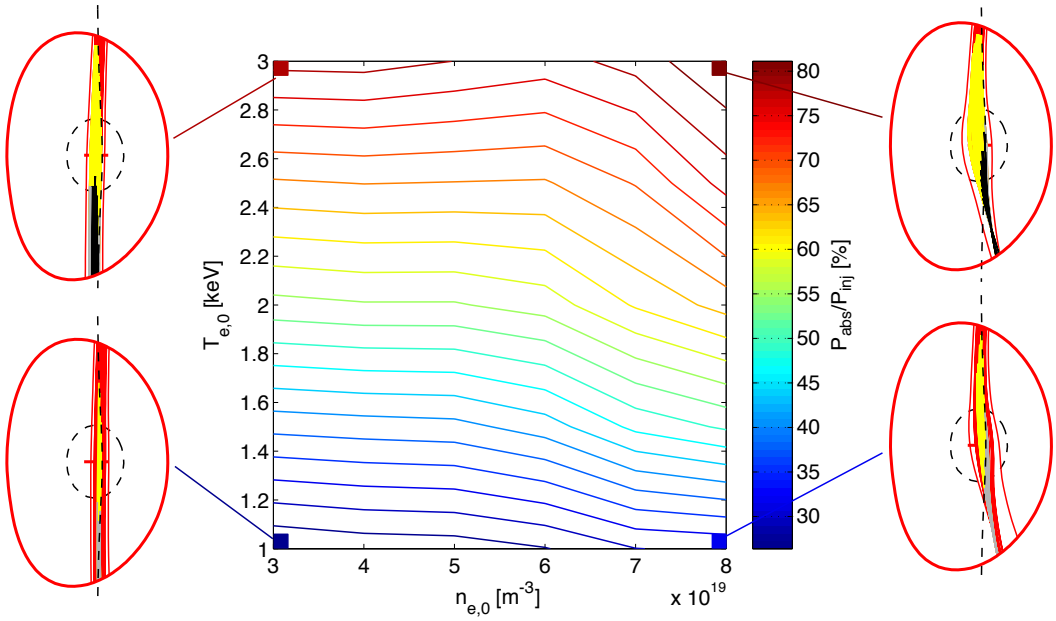

Figure 12. The contour plot of the absorption calculated by TORAY-GA in the density and temperature domain. The temperature and density profiles have been taken as fits on Thomson scattering measurement as can be seen on Figure 20. The profiles have been changed multiplying them by the appropriate factor. In the corners, the poloidal view of the beam trajectory for the four extreme points of the (n_e, T_e) domain (small squares). In these 4 pictures, the yellow area corresponds to the region where the beam is mainly absorbed.

expected, the absorption increases with the temperature and the density. The absorption increase due to the density is very weak compared with the temperature effect. The only way to obtain more than 70% absorption is to reach high enough temperature, more difficult at high density. The beam trajectory calculated by TORAY-GA is shown in the poloidal views in the corners of Figure 12 for the four extremities of the contour plot. The yellow area corresponds to the region where the power is mainly absorbed and the resonance layer broadening can clearly be seen by comparing the upper to the lower

poloidal views. The poloidal views on the right show the strong refraction effect on the beam trajectory, especially in the lower part of the plasma cross section. In these cases the WKB approximation is probably not valid but this should not affect the absorption results since the beam is mainly absorbed in the upper part of the plasma.

These calculations will be compared with experimental results in section 4 where it will be shown that the agreement on the optimal angle $\theta_{l,opt}$ is good. Additional comparisons are presently under study with other codes such as a beam tracing code taking into account diffraction effects [15, 16, 17] , and a code which takes into account hot plasma effects for the ray-tracing [18].

3. Experimental setup

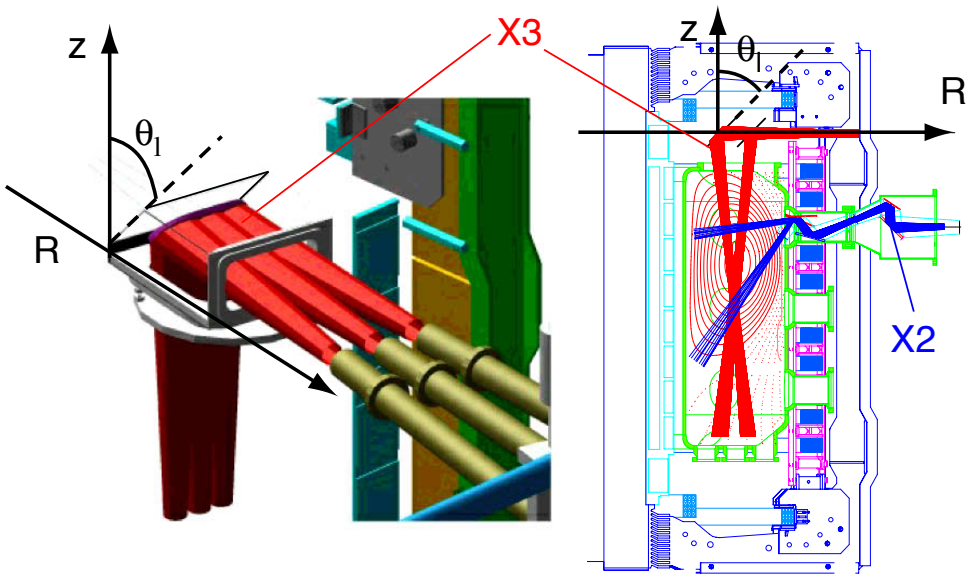

Figure 13. The poloidal view of TCV shows the launcher flexibility for vertical injection (X3) and lateral injection (X2). The X3 launcher can move in the radial direction between 800 mm and 960 mm (R_0 = 880 mm on TCV) from shot to shot. The launcher poloidal angle θ_l can vary in the range $40^o - 50^o$ during the shot.

The X3 heating system [19] is composed of three 118 GHz gyrotrons, each providing 450 kW of power in the torus with a maximum pulse length of 2 s in TCV. The wave is linearly polarized and coupled to an evacuated HE_{11} transmission line (63.3 mm diameter) via a Radio Frequency Conditioning Unit (RFCU). The three wave guides radiate the RF beams onto a single elliptical mirror as shown in Figure 13. This mirror is made of copper and has a 700 mm focal length, focusing the beam inside the plasma. Assuming a gaussian power distribution, its minimum waist is $w_0 = 23$ mm (Equation (13)). The mirror can be steered radially from 800 to 960 mm ($R_0 = 880$ mm on TCV) from pulse to pulse and the poloidal injection angle θ_l can vary from 40 to 50 degrees during the shot with a maximum speed of 20 deg/s.

4. Experiments

In the present section, a first set of experiments is presented to illustrate the launcher's poloidal angle sensitivity and the influence of the temperature and density on the absorption with and without X2 preheating. A second set of experiments shows that the X3 absorption is increased as the power is increased up to the maximum injected power, until full single pass absorption is obtained. All the experimental results are compared with the TORAY-GA calculations.

As discussed in section 2, first the X3 absorption is expected to increase with the temperature and secondly, the shift effect associated with T_e implies that the optimal launcher angle $\theta_{l,opt}$ increases (displacement toward the HFS). To verify these two effects, a set of experiments was performed, injecting 450 kW X3 and sweeping θ_l during the shot from 45.5^o to 47.5^o (see Figure 14 d)). The θ_l sweep causes the beam to pass through the resonance layer, determining the optimal angle $\theta_{l,opt}$ from the Soft X-ray (SXR) measurement (Figure 14 c). X2 ECH, launched from the LFS into the plasma center, has been used to control the temperature as shown in Figure 14. This scenario

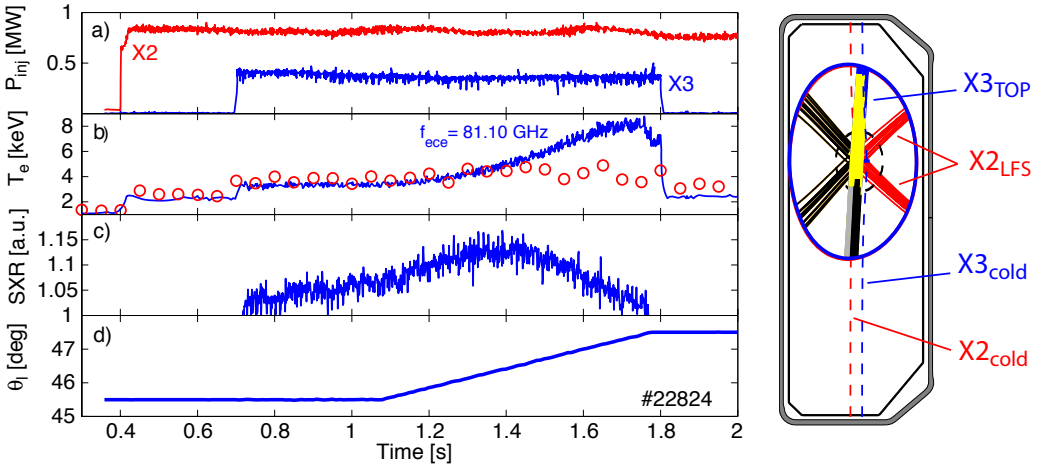

Figure 14. a) Injected power for X3 (450 kW) and X2 (900 kW). b) The bulk temperature from Thomson scattering measurement (empty circles) super-imposed on the ECE radiative temperature measured from the HFS. c) The Soft X-ray emission measured along a vertical view line ($SXR \propto T_{e,bulk}$). d) The launcher poloidal angle θ_l, swept during the shot.

has been repeated varying the X2 power from 0 to 1.35 MW (3 gyrotrons). The electron temperature is measured by Thomson scattering (open circles on Figure 14 b)) and the SXR signal gives a relative measurement of the fast time evolution, since SXR varies monotonically with T_e. It has been verified that the photodiode signal is dominated by the bulk temperature (at constant density) when the filter is a 50 μm Be window. X2 ECCD experiments have shown, by comparing the signal with a hard X-ray camera, that the signal is dominated by the SEP only if the filter is at least a 300 μm Al window (Photon energy > 15 keV). The central ($f_{ece} = 81.1$ GHz) ECE radiative temperature

measured on the HFS, T_{rad} (plain curve on Figure 14 b)) indicates the presence of an SEP if it deviates from Thomson (circles on Figure 14 b)) [14]. As discussed in reference [14], for the SEP shown in Figure 14, the spatial resolution degradation of the ECE-HFS radiometer due to the deviation from the Maxwellian distribution function is of the order of 1 cm. The comparison of T_{rad} for this ECE channel with the central Thomson measurement is pertinent. During the sweep, when θ_l increases, T_{rad} becomes higher than $T_{e,bulk}$ meaning that the SEP is becoming bigger. As shown on Figure 15 a), the SXR signal yields the optimal angle $\theta_{l,opt}$ for the bulk heating whereas T_{rad} yields the optimal angle $\theta_{l,opt}^{sup}$ for SEP heating/generation. Since $\theta_{l,opt}^{sup} > \theta_{l,opt}$ and since the optimum of the absorption on the bulk is close to the cold resonance, we can conclude that at the optimum angle for the SEP formation, a substantial fraction of power is absorbed by the nonthermal electrons owing to the relativistic shift (see section 2.2). Figure 15 b) shows $\theta_{l,opt}$ (blue curve) and $\theta_{l,opt}^{sup}$ (green curve) as functions of the X2

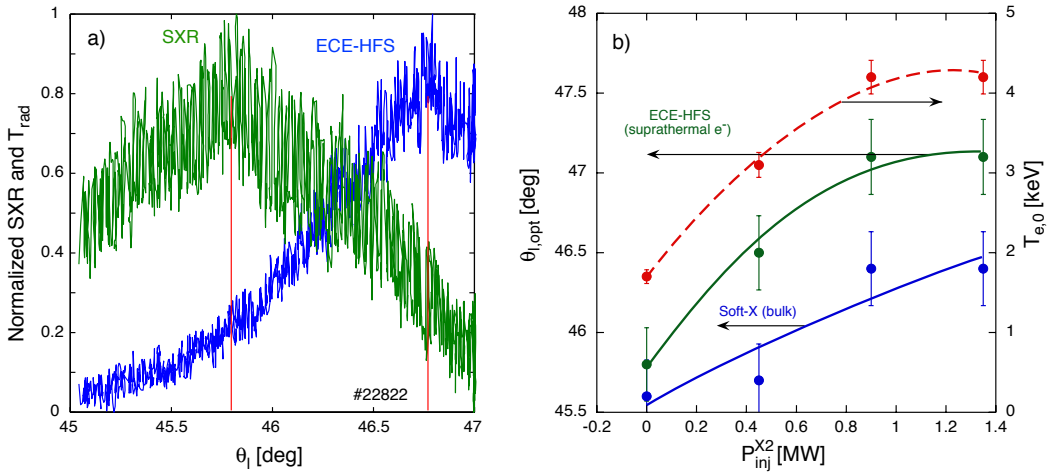

Figure 15. a) The SXR and T_{rad} from the ECE-HFS measurements give, during the θ_l sweep, the optimal angles for bulk heating and SEP formation respectively. b) The optimal angle given by the radiative and bulk temperatures increase with the X2 injected power. The bulk temperature increase with power is also shown (dashed line).

injected power. The central bulk temperature $T_{e,0}$ associated with these optimal angles is also shown (dashed curve). Comparing the measured $\theta_{l,opt}$ with the shift effect shown in Figure 6 associated with the temperature, and taking into account that the model is approximated in a 1D slab geometry, the experimental results are in good agreement with the model since the measurement gives $\frac{d}{dT_e}(\Delta\theta) \simeq 0.4$ deg/keV.

The other two main parameters discussed in section 2 were the X3 absorption sensitivity $\delta\theta_l$ on the launcher poloidal angle and the optimal density, expected to be $n_e = 7 \cdot 10^{19}$ m^{-3}. A set of experiments has been performed to test these predictions and TORAY-GA simulations with 450 kW X3 power injected in a L-mode plasma target without X2 preheating. The launcher poloidal angle θ_l was swept during the pulse from 42^o to 48^o to pass through the maximum of absorption. Figure 16 shows the poloidal view of the plasma target and the ray trajectories, calculated by TORAY-GA,

corresponding to the launcher's poloidal angle range. The radial position of the mirror was fixed on the LFS of the cold resonance at $R = 935$ mm. The sweep scenario was repeated for various central densities from $n_{e,0} = 3.1 \cdot 10^{19}$ m^{-3} to $n_{e,0} = 8.0 \cdot 10^{19}$ m^{-3}. Figure 16 shows the core-weighted temperature, deduced from the soft X-ray emission measurement (T_e-X, two foil method [20]) along a central vertical view line, as a function of θ_l for three densities: a) $n_{e,0} = 3.1 \cdot 10^{19}$ m^{-3}, b) $n_{e,0} = 5.5 \cdot 10^{19}$ m^{-3} and c) $n_{e,0} = 8.0 \cdot 10^{19}$ m^{-3}. The X3 absorption calculated by TORAY-GA (red dots) is superimposed on the T_e-X signal. For each θ_l, the corresponding temperature and density

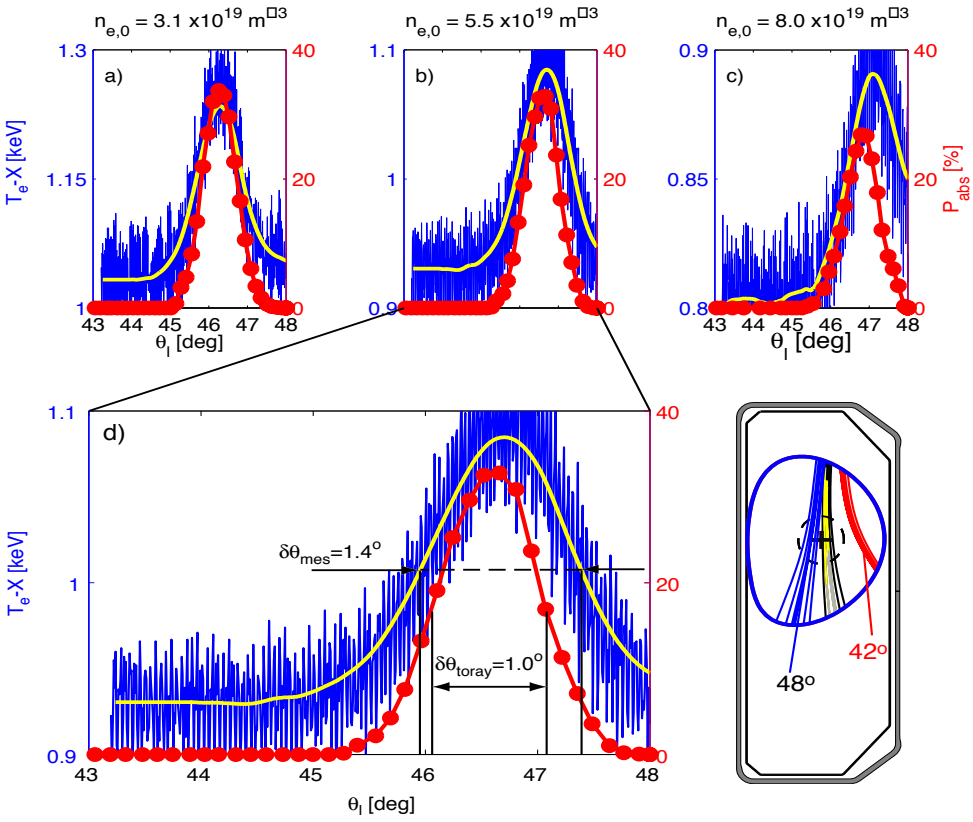

Figure 16. The global temperature deduced from the T_e-X measurement gives qualitatively the absorption efficiency (blue lines). By sweeping θ_l, the optimal angle $\theta_{l,opt}$ can be determined using the smoothed T_e-X signal (yellow lines). The absorption calculated by TORAY-GA is superimposed on T_e-X (red lines with dots). The poloidal view of the plasma cross-section shows the beam trajectories during the sweep. The angle sweep scenario has been repeated for three central densities a) $n_{e,0} = 3.1 \cdot 10^{19}$ m^{-3}, b) $n_{e,0} = 5.5 \cdot 10^{19}$ m^{-3} and c) $n_{e,0} = 8.0 \cdot 10^{19}$ m^{-3}. d) The launcher poloidal angular tolerance $\delta\theta$ from T_e-X and P_{abs} .

profiles, fitted to the Thomson scattering measurements, have been used as inputs to the TORAY-GA code. The optimal launcher angle $\theta_{l,opt}$ can be experimentally determined taking the maximum of the T_e-X measurement, smoothed using a digital low-pass filter (yellow line). This measurement is compared with $\theta_{l,opt}$ determined from the maximum of the absorption calculated by TORAY-GA. Figure 17 a) shows that $\theta_{l,opt}$ increases as

the central density $n_{e,0}$ increases for both the measurements and the simulations and that the two are in good agreement. $\theta_{l,opt}$ increases with the density because it has to compensate the refraction effect on the beam trajectory. The vertical bars on Figure 17 represent the launcher poloidal tolerance $\delta\theta_l$. The measured angular tolerance $\delta\theta_{mes}$ is determined taking the full width at half maximum (FWHM) of the smoothed T_e-X signal as shown on Figure 16 d). $\delta\theta_{mes}$ is compared to $\delta\theta_{toray}$ determined by the FWHM of the TORAY-GA absorption curve. As illustrated on Figure 17 a), the tolerance does not depend on the density and $\delta\theta_{mes} = 1.4^o > \delta\theta_{toray} = 1.0^o$ systematically. This discrepancy may be explained by the fact that the gaussian beam model does not take diffraction effects into account. However, both $\delta\theta_{mes} > \delta\theta_l$ and $\delta\theta_{toray} > \delta\theta_l$ where $\delta\theta_l$ is the tolerance calculated in the 1D slab model in section 2 as could be expected.

Independently of these quantitative details, the strong sensitivity of the X3 absorption on the density (refraction) and temperature (relativistic shift) implies that a real time feedback control on the launcher poloidal angle is required for maintaining a maximal absorption during a discharge. Real time feedback control has been developed based on a synchronous demodulation techniques which exploits a perturbation of the T_e-X signal induced by the launcher's poloidal angle sinusoidal modulation. The error signal obtained from the T_e-X response is then fed to a PID analog controller [21]. This system is presently being tested on TCV.

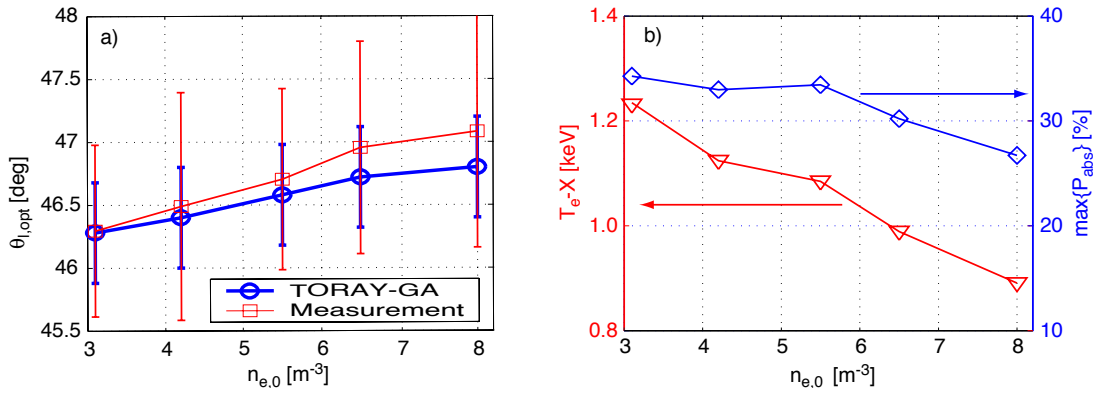

Figure 17. a) The launcher optimal angle versus the central density $n_{e,0}$ has been obtained from T_e-X measurement (squares) and from TORAY-GA calculation (circles). The vertical bars represent $\delta\theta$ which does not depend on the density. b) The absorbed power, calculated by TORAY-GA at $\theta_{l,opt}$ (diamonds curve) is compared to the T_e-X signal measured at $\theta_{l,opt}$ (triangles).

Figure 17 b) shows T_e-X measured at the optimal angle as a function of the central density. The maximum absorption, $max\{P_{abs}\}$ calculated by TORAY-GA using experimental input parameters at $\theta_{l,opt}$ conditions is super-imposed on this curve. The absorption decreases with the density because the temperature decreases. The density effect on the absorption is too low, hence not visible compared with the temperature effect. This confirms the predictions given by the contour plot in Figure 12.

As described, for X3 top-launch, the optical depth $\tau_{X3,top}$ scales linearly with the

electron temperature. The bulk temperature increases monotonically with the additional X3 absorbed power, even assuming power degradation of the global confinement time. Experiments have been performed varying the X3 injected power from 450 kW (1 gyrotron) to 1350 kW (3 gyrotrons) to determine how the X3 absorption is increased. The experiment is illustrated in Figure 18 in which the plasma target is similar to the previously discussed experiments and the central density is $n_{e,0} = 4 \cdot 10^{19}$ m^{-3}. The optimal launcher angle is first determined by sweeping θ_l and the discharge is then repeated injecting the X3 power at the fixed angle $\theta_{l,opt}$. In the middle of the 1.35 MW, 1s ECH phase, one gyrotron (0.45 MW) is fully modulated at 237 Hz for 200 ms to determine the X3 absorption measured via the diamagnetic flux variation associated with the modulation [22]. Figure 18 b) shows the central bulk temperature measured by Thomson scattering (open circles) and the radiative temperature determined from the HFS-ECE measurement. During the ohmic phase, the amplitude of both signals

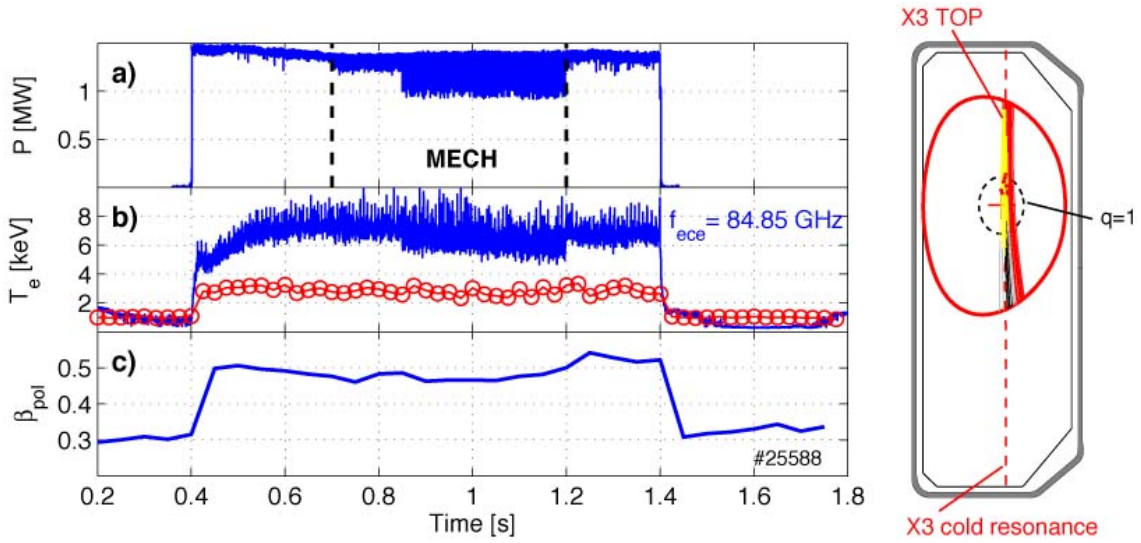

Figure 18. a) 1.5 MW X3 is injected during 1 second and the power of one gyrotron is fully modulated between 0.9 and 1.2 s, b) the radiative temperature determined from the HFS-ECE measurement (line) is super-imposed on the Thomson central temperature (circles), c) The β_{pol} is significantly increased by the X3 heating.

is equal, indicating the absence of an SEP. When the X3 power is turned on, the bulk temperature increases on an energy confinement time scale whereas the SEP generated by the X3 wave itself is formed on a significantly longer time scale. The presence of an SEP can strongly modify the X3 absorption conditions (section 2.2). Figure 19 shows the measured single pass absorption (squares) as a function of the total plasma power, $P_{tot} = P_{oh} + P_{ech}$, where the ohmic power $P_{oh} = I_p \cdot V_{loop}$. As expected, the measured X3 absorption increases with the central temperature. By injecting the maximum available X3 power at TCV ($P_{inj} = 1350$ kW), full single pass absorption is obtained and the central temperature reaches $T_{e,0} = 2.7$ keV (Figure 19 circles). This figure suggests that if $T_e > 2$ keV, 80% absorption can be obtained as predicted by the 1D slab geometry

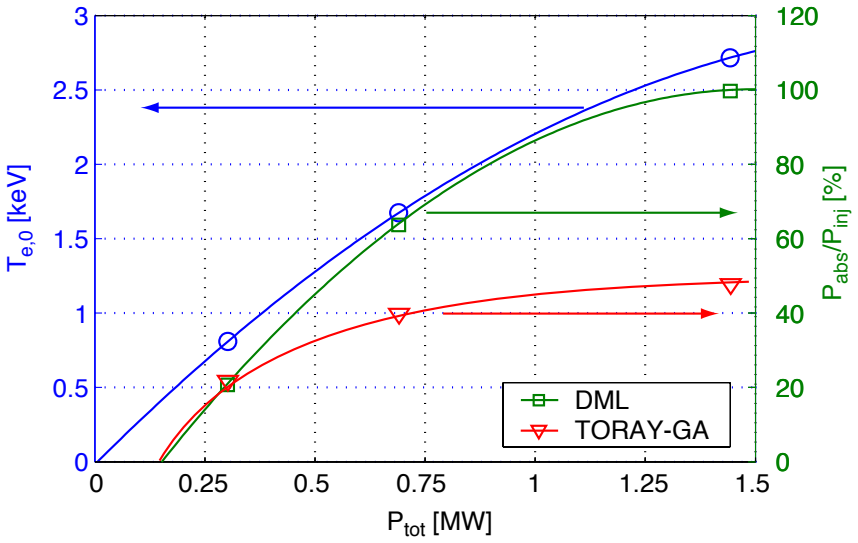

Figure 19. The central temperature $T_{e,0}$ from Thomson measurement that has been obtained during X3 ECH is plotted (circles) as a function of the total power $P_{tot} = P_{oh} + P_{ech}$. The squares represent the measured single pass absorption (right axis). and are compared to the calculated ones by TORAY-GA (triangles).

model (see Figure 3 in section 2). The absorption measurement is compared with the TORAY-GA calculations (Figure 19 triangles). A discrepancy is observed between the two curves especially at highest P_{inj}. This may be partly explained by the presence of an SEP generated by the X3 wave itself as in Figure 18. With an angular tolerance of $\delta\theta_{toray} = 1.0^o$, part of the discrepancy may also be associated with the accuracy of the reconstructed equilibrium, especially concerning the plasma radial position or with an inaccuracy of the launcher.

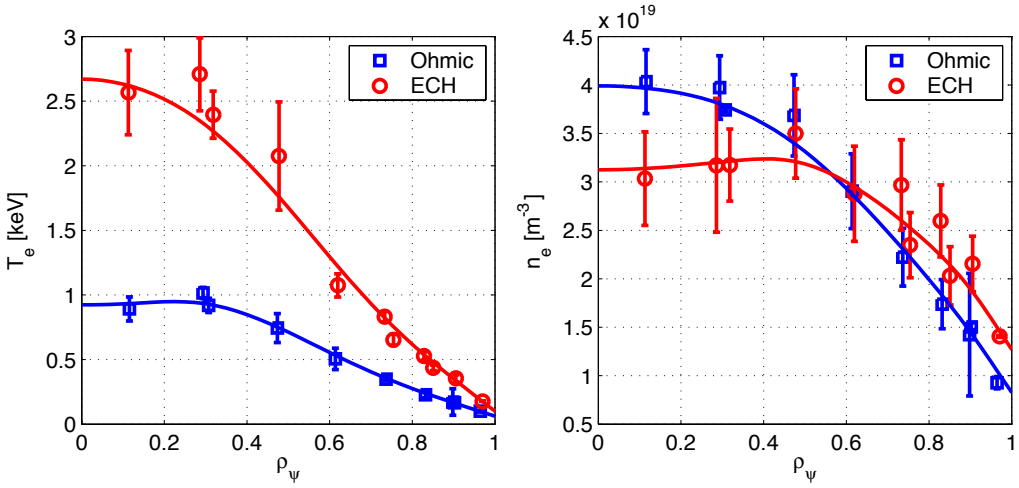

Figure 20. The temperature and density profiles measured with the Thomson scattering diagnostic for both ohmic and ECH phases. The profiles are time averaged over 100 ms for the ohmic phase and 200 ms for the ECH phase

However, the global electron energy W_e is increased by a factor 2.5 when full single pass absorption is obtained and the associated temperature and density profiles are shown in Figure 20. The ohmic profiles (squares) are time averaged during 100 ms before the X3 is turned on and the profiles during the ECH phase (circles) are time averaged from the start of the ECH pulse until the modulation (MECH) phase. At the X3 power switch on, a clear flattening of the density profile is observed. This "pump-out" phenomenon has also been observed on X2 ECH and ECCD experiments on TCV [23, 24] as well as during ECH/ECCD experiments on ASDEX Upgrade [25].

5. Conclusion

A top-launch X3 ECH system has been installed on TCV in order to heat high density plasmas. The X3 absorption is theoretically predicted to be strongly sensitive to the launcher's poloidal angle. The sensitivity decreases in the presence of a suprathermal electron population because the resonance layer width broadens due to the relativistic shift. Experimental results and ray-tracing calculations using TORAY-GA show that the launcher's poloidal angle tolerance is of the order of 1^o. The launcher's tolerance makes no distinction between the temperature dependence and the strict geometrical dependence of the absorption. In order to optimize the X3 absorption during a discharge, a real time feedback control using a synchronous demodulation technique and PID controller is being tested. The optimal launcher angle predicted by TORAY-GA is in good agreement with the measurement. At the maximum available X3 injected power of 1350 kW, full single pass absorption has been measured, whereas TORAY-GA predicts only 50% absorption. This discrepancy is partly attributed to the presence of suprathermal electrons generated by X3 itself. When X3 is fully absorbed, a flattening of the density profile is observed as already seen during X2 ECH/ECCD experiments on TCV and ASDEX Upgrade.

Comparison between the linear ray-tracing code TORAY-GA and more complex models including diffraction (beam tracing code ECWGB [15, 16, 17]) and hot plasma effects on the ray tracing (GENRAY [18]) is presently underway.

6. Acknowledgement

This work was partly supported by the Swiss National Science Foundation.

A special thanks to S. Coda and J. B. Lister for their help and pertinent criticism.

7. References

[1] T. P. Goodman and al. *Proc. in 19^{th} Symposium on Fusion Technology, Amsterdam (Holland)*, 1994.

[2] R.L. Meyer, I. Fidone, G. Granata, and E. Mazzucato. *Proc. in 7^{th} Top. conf. on app. of RF power to plasmas, Kissimee, AIP*, 157:73, 1987.

[3] A. Pachtman, S. M. Wolfe, and I. H. Hutchinson. *Nucl. Fusion*, 27:1283, 1987.
[4] J.-L. Ségui and al. *Nucl. Fusion*, 36:237, 1996.
[5] N. Yanagi, S. Morimoto, M. Sato, S. Kobayashi, M. Iima, S. Besshou, H. Nakamura, K. Ichiguchi, K. Hanatani, and T. Obiki. *Nucl. Fusion*, 31:261–271, 1991.
[6] U. Gasparino, H. Idei, S. Kubo, N. Marushchenko, and M. Romé. *Nucl. Fusion*, 38:223–235, 1998.
[7] J. N. Talmadge, H. Zushi, S. Sudo, T. Mutoh, M. Sato, T. Obiki, O. Motojima, A. Liyoshi, and K. Uo. *Phys. Rev. Letter*, 53:33–36, 1983.
[8] R. H. Cohen. *Phys. Fluids*, 30:2442, 1987.
[9] K. Matsuda. *IEEE Trans. Plasma Sci.*, 17:6, 1989.
[10] Y. R. Lin-Liu and et al. *Proc. in 26th EPS conference on Plasma Physics and Controlled Fusion, Maastricht*, 23J:1245, 1999.
[11] E. Nelson-Melby, S. Alberti, T. Goodman, M. Henderson, and P. Nikkola. *Proc. in 30th EPS conference, St Petersburg*, P3.210, 2003.
[12] M. Bornatici and al. *Nucl. Fusion*, 23:1153–1257, 1983.
[13] S. Alberti and al. *Nucl. Fusion*, 42:42–45, 2002.
[14] P. Blanchard, S. Alberti, S. Coda, H. Weisen, P. Nikkola, and I. Klimanov. *Plasma Phys. Control. Fusion*, 44:2231, 2002.
[15] S. Nowak and A. Orefice. *Phys. Fluids*, 5:1242, 1993.
[16] S. Nowak and A. Orefice. *Phys. Fluids*, 1:1945, 1994.
[17] S. Cirant, S. Nowak, and A. Orefice. *J. Plasma Physics*, 53:354–364, 1995.
[18] A. P. Smirnov and R. W. Harvey. *Bull. Amer. Phys. Soc.*, 40:1837, 1995.
[19] J.-Ph. Hogge, S. Alberti, L. Porte, and G. Arnoux. *Nucl. Fusion*, 43:1353–1360, 2003.
[20] J. Kiraly, M. Bitter, P. Efthimion, S. Von Goeler, B. Grek, K. W. Hill, D. Johnson, K. McGuire, N. Sauthoff, S. Sesnic, F. Stauffer, G. Tait, and G. Taylor. *Nucl. Fusion*, 27:397, 1987.
[21] G. Arnoux, S. Alberti, E. Nelson-Melby, L. Porte, P. Blanchard, J.-Ph Hogge, and TCV Team. *Proc. in IAEA Technical Meeting on ECRH for ITER*, Kloster Seeon, Germany, June 14-16, 2003.
[22] A. Manini, J.-M. Moret, S. Alberti, T. P. Goodman, and M. A. Henderson. *Pasma Phys. Control. Fusion*, 44, 2002.
[23] H. Weisen, I. Furno, and al. *Nucl. Fusion*, 42:136, 2002.
[24] A. Zabolotsky, H. Weisen, and TCV Team. *Plasma Phys. Control. Fusion*, 45:735, 2003.
[25] C. Angioni, A.G. Peeters, X. Garbet, A. Manini, F. Ryter, and ASDEX Upgrade Team. *Nucl. Fusion*, To be published, 2004.